CHEMISTRY

Two-dimensional polymers with versatile functionalities via gemini monomers

Yang Li[1], Huimin Gao[2], Huan Yu[3], Ke Jiang[1], Hua Yu[1], Yang Yang[1], Yu Song[1], Wenke Zhang[1], Hengchong Shi[3], Zhongyuan Lu[2], Kun Liu[1,4]*

Two-dimensional synthetic polymers (2DSPs) are sheet-like macromolecules consisting of covalently linked repeat units in two directions. Access to 2DSPs with controlled size and shape and diverse functionality has been limited because of the need for monomers to retain their crystallinity throughout polymerization. Here, we describe a synthetic strategy for 2DSPs that obviates the need for crystallinity, via the free radical copolymerization of amphiphilic gemini monomers and their monomeric derivatives arranged in a bilayer at solid-liquid interfaces. The ease of this strategy allowed the preparation of 2DSPs with well-controlled size and shape and diverse functionality on solid templates composed of various materials with wide-ranging surface curvatures and dimensions. The resulting 2DSPs showed remarkable mechanical strength and have multiple applications, such as nanolithographic resist and antibacterial agent. The broad scope of this approach markedly expands the chemistry, morphology, and functionality of 2DSPs accessible for practical applications.

INTRODUCTION

Two-dimensional synthetic polymers (2DSPs) constructed with monomeric repeat units joined by covalent bonds in two directions have attracted a wide range of interest in basic scientific research and potential impactful technologies (*1*–*3*). Because of their 2D network structure, the properties of 2DSPs differ strongly from those of 1D and 3D polymers. However, the design and synthesis of 2DSPs present far greater challenges compared to their 1D counterparts. Various synthetic approaches have been explored toward the preparation of these fascinating sheet-like macromolecules, with the topochemical solid-state polymerization approach being the most successful one to date (*4*–*6*). Topochemical solid-state polymerization is achieved by crystallizing monomers into single crystals or crystalline Langmuir-Blodgett films and subsequent in situ polymerization with topochemical reactions. Schlüter and co-workers (*5*, *6*) have made substantial inroad on this synthetic method, yielding 2DSPs with well-characterized periodic structures, large areas, and gram-scale yields. Nevertheless, the prerequisite of crystalline monomers in the synthesis of 2DSPs continues to hinder the introduction of functional groups and controlled architectures. In addition, challenges in the design and preparation of the monomers, as well as control over the crystallization processes must be overcome for this approach for 2DSPs to be useful for practical purposes (*4*–*6*).

Using noncrystallization methods in an alternative synthetic strategy toward 2DSPs can effectively avoid the aforementioned problems. Pioneering studies on noncrystallization strategy can be traced back to the works of Stupp and co-workers (*7*), in which monomers with two reaction sites were polymerized in smectic phase. Other examples involving specially designed phosphocholine monomers via cross-linking in multilayer vesicles or photopolymerization in substrate-supported bilayers have also made important contributions both experimentally and conceptually (*8*–*11*). However, these methods do not lead to freestanding monolayers of 2DSPs, which is an important step in the search for well-defined 2DSPs (*4*–*6*, *12*). Consequently, successful applications of the noncrystallization strategy for 2DSPs are urgently needed to expand the synthetic methods and expand on the accessible architectures and functionalities of 2DSPs.

In this work, we used the in situ free-radical polymerization of the amphiphilic gemini monomer MA-11-2-11-MA [*N*,*N*′-bis(11-(methacryloyloxy)undecyl)-*N*,*N*,*N*′,*N*′-tetramethylethane-diaminium bromide] arranged in a bilayer on a solid-liquid interface to generate a highly cross-linked single bilayer of freestanding 2D *net*-poly(MA-11-2-11-MA) (Fig. 1A). We proved that 2DSPs can be synthesized from a dynamic bilayer of gemini monomers without the use of crystal lattices. Both of the rotating-frame Overhauser effect spectroscopy (ROESY) study and dissipative particle dynamics (DPD) simulation suggested that gemini MA-11-2-11-MA underwent a polymerization-induced structural self-organization process, resulting in the formation of *net*-poly(MA-11-2-11-MA) with a regular sublayer structure. Furthermore, the self-adaptability of gemini MA-11-2-11-MA facilitated the access to 2D *net*-poly(MA-11-2-11-MA) with diverse shapes in a templated process; the templates ranged from submicroscopic to microscopic scale and can be removed without affecting the overall shape of the 2DSP. Functionalized 2DSPs can be made in a single step via copolymerization of gemini MA-11-2-11-MA with various monomeric derivatives, MA-11-F (F represents functional group). The functionalized *net*-poly(MA-11-2-11-MA) can be used as surface modifiers on a wide range of materials such as metal, plastic, silica, and cotton fibers, while the modified surfaces have promising potential biomedical applications as antibacterial materials. With this major advance, 2DSPs are within reach of practical applications in the real world.

RESULTS

Preparation and characterization of *net*-poly(MA-11-2-11-MA)

A large area of 2D *net*-poly(MA-11-2-11-MA) as a single bilayer was synthesized on a solid-liquid interface (Fig. 1A). The positively charged gemini monomers MA-11-2-11-MA were initially adsorbed onto a negatively charged silicon wafer (2.0 cm by 2.0 cm) electrostatically by dipping the wafer in an aqueous solution of the monomer (5.0 mM).

[1]State Key Laboratory of Supramolecular Structure and Materials, College of Chemistry, Jilin University, Changchun 130012, China. [2]State Key Laboratory of Supramolecular Structure and Materials, Institute of Theoretical Chemistry, Jilin University, Changchun 130021, China. [3]State Key Laboratory of Polymer Physics and Chemistry, Changchun Institute of Applied Chemistry, Chinese Academy of Sciences, Changchun 130022, China. [4]State Key Laboratory of Applied Optics, Changchun Institute of Optics, Fine Mechanics and Physics, Chinese Academy of Sciences, Changchun 130021, China.
*Corresponding author. Email: kliu@jlu.edu.cn

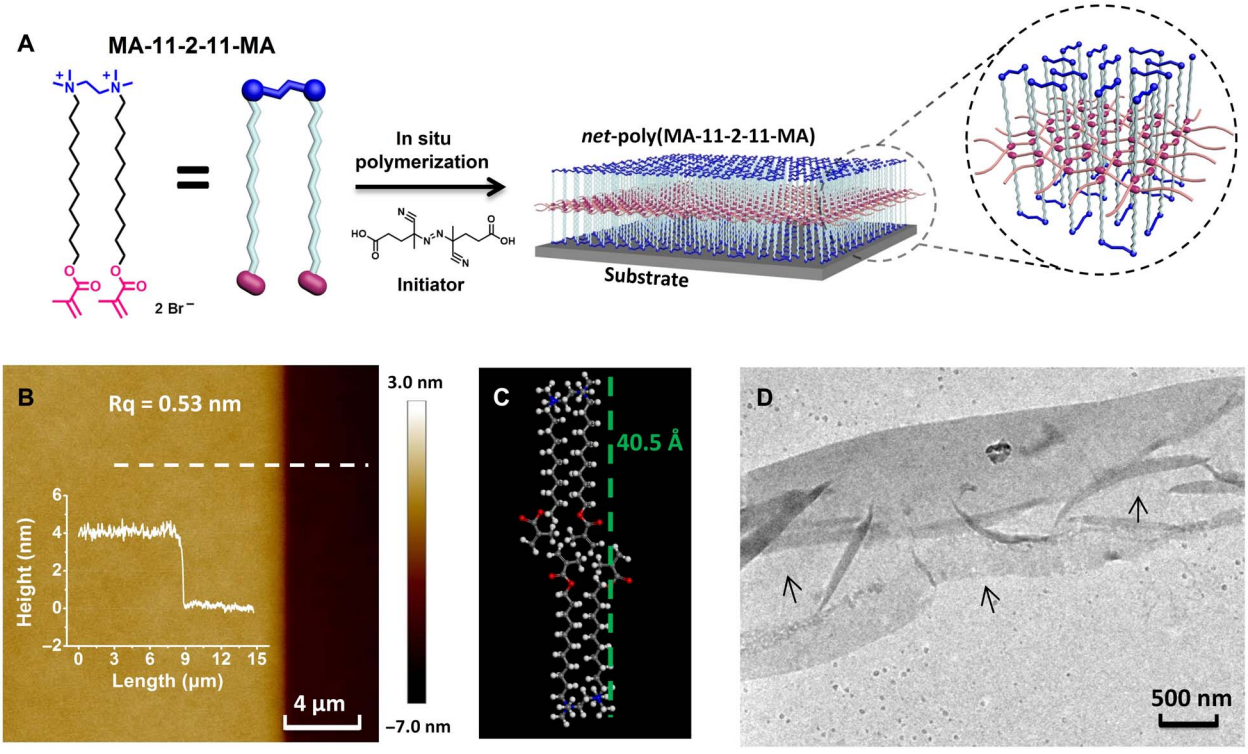

Fig. 1. Preparation and characterization of 2D *net*-poly(MA-11-2-11-MA). (**A**) Schematic illustration of the molecular structure of gemini monomer MA-11-2-11-MA and 2D *net*-poly(MA-11-2-11-MA). (**B**) AFM image and height analysis of the 2D *net*-poly(MA-11-2-11-MA) on the silicon substrate. Rq, root mean square roughness. (**C**) Simulation of the bilayer thickness with vertically arranged MA-11-2-11-MA monomers using Materials Studio. (**D**) TEM image of the freestanding film of 2D *net*-poly(MA-11-2-11-MA).

As this concentration is above its critical micelle concentration (CMC) of 4.3 mM (fig. S1A), the MA-11-2-11-MA monomers formed a uniform bilayer covering the silicon wafer within 10 min of incubation. The double-layered adsorption behavior of MA-11-2-11-MA on the silicon wafer was confirmed by its adsorption isotherm (fig. S1B). Subsequently, the bilayer of MA-11-2-11-MA was cross-linked using free-radical polymerization at 65°C with a water soluble initiator, 4,4′-azobis(4-cyanopentanoic acid) (ACVA). The negative charge of ACVA facilitated the penetration of the MA-11-2-11-MA bilayer, allowing the polymerization of methacrylate groups in the middle of the bilayer. During the polymerization, covalent bonds formed between the methacrylate groups from both the upper and lower layers of MA-11-2-11-MA, threading the MA-11-2-11-MA monomers into 2D networks. The 11-2-11 units between the two methacrylate groups in MA-11-2-11-MA, acting as staples, formed cross-links above and below the poly(methacrylate) sublayer, resulting in a highly cross-linked structure (Fig. 1A). The conversion ratio of MA-11-2-11-MA was close to 100%, which was important for the formation of a highly cross-linked 2D network (fig. S2, A and B).

After polymerization, the film of *net*-poly(MA-11-2-11-MA) was washed with deionized (DI) water thoroughly. Atomic force microscopy (AFM) characterization at randomly selected positions showed that the 2D *net*-poly(MA-11-2-11-MA) film uniformly covered the silicon substrate (fig. S2C). The root mean square roughness of the *net*-poly(MA-11-2-11-MA) film with an area of 10 μm by 10 μm was determined to be 0.53 nm, indicative of a flawless and smooth surface. To measure the film thickness, we removed a fraction of the *net*-poly(MA-11-2-11-MA) film using oxygen reactive ion etching (RIE) with a silicon wafer as the hard mask. AFM height analysis at the edge of the film gave a thickness of approximately 4.0 nm for the 2D *net*-poly(MA-11-2-11-MA) film (Fig. 1B). This value matched well with twice the height of the MA-11-2-11-MA molecule (Fig. 1C; calculations in Materials Studio gave a height of 40.5 Å). Together, the AFM and calculation results confirmed a vertical arrangement of the MA-11-2-11-MA molecules in the bilayer with the methacrylate groups aligned in the center of the bilayer. To further study the structure of the MA-11-2-11-MA bilayer, we used Fourier transform infrared (FT-IR) spectroscopy to verify the orientation of the MA-11-2-11-MA molecules in the bilayer (*13*). The intensities of the C—H stretching vibration peak (at 2800 to 2980 cm^{-1}) and the C—H in-plane bending vibration peak (at 1430 to 1510 cm^{-1}) of C_{11} alkyl chain in the grazing-angle reflection mode are notably weaker than those in the transmission mode (fig. S3B). This is the result of a mismatch between the direction of the vibrating electric field of the polarized infrared light and the dominant orientation of hydrocarbon bonds in the aligned alkyl chain of MA-11-2-11-MA that are perpendicular to the substrate, as observed in the study of similarly oriented bilayers (*14*). This result further supports the vertical arrangement of MA-11-2-11-MA in the bilayer and is consistent with results from AFM. In addition, the chemical composition of the *net*-poly(MA-11-2-11-MA) was analyzed by x-ray photoelectron spectroscopy (XPS). The XPS spectra of C1s of 2D *net*-poly(MA-11-2-11-MA) on the silicon wafer (C—C/C—H, 60.1%; C—OH/C—OR, 31.9%; C═O, 3.3%; and C—N, 4.7%) was consistent with that of poly(MA-11-2-11-MA) obtained from the polymerization of MA-11-2-11-MA in bulk (C—C/C—H, 61.0%; C—OH/C—OR, 31.4%; C═O, 3.2%; and C—N, 4.4%),

confirming the existence of 2D *net*-poly(MA-11-2-11-MA) on the silicon wafer (fig. S4).

Next, a freestanding film of *net*-poly(MA-11-2-11-MA) was obtained using the same polymerization method. Instead of silicon, an ultrathin slice of mica was used as a substrate and subsequently removed by etching with hydrofluoric acid. A representative transmission electron microscopy (TEM) image of a freestanding film of *net*-poly(MA-11-2-11-MA) (Fig. 1D) shows that the unfolded parts (indicated with arrows) are extremely thin, with a contrast that is almost indistinguishable from that of the carbon film of the TEM grid. The mechanical strength of the thin *net*-poly(MA-11-2-11-MA) film was high enough to maintain structural integrity in solution. The quantitative mechanical strength of 2D *net*-poly(MA-11-2-11-MA) was determined with AFM indentation measurement according to the reported method (fig. S5) (*15*). The in-plane elastic modulus (E^{2D}) of *net*-poly(MA-11-2-11-MA) was measured to be 126.3 ± 25.7 N/m, which was about one-third of the E^{2D} of graphene (340 N/m) and comparable to those of 2D materials (*16*, *17*). This result further supported the highly cross-linked nature of *net*-poly(MA-11-2-11-MA).

Structual regulation of MA-11-2-11-MA bilayer during the polymerization

A gemini surfactant consisting of two hydrophilic heads, a linker between the heads, and two hydrophobic tails allows for the rational design of each component for targeted self-assembled structures. MA-11-2-11-MA is an example of such surfactant, which was designed to form a flat bilayer that would allow effective cross-linking. To come up with an optimal structure, we first considered a number of parameters relevant to surfactant packing. The assembly geometry of the gemini surfactant at a hydrophilic solid-water interface is greatly affected by its packing parameter, which is defined as $P = v/la_0$ (v represents the volume of the hydrocarbon chains, l represents the critical chain length, and a_0 represents the optimal head-group area) (*18*). To achieve a flat bilayer structure, a relatively high R is required. A series of gemini surfactants with the structure of 12-n-12 (n = 2, 4, 6, and 8) were evaluated; the results indicated that the combination 12-2-12 has the smallest optimal head-group area a_0 and the highest packing parameter P, and it is the only one that forms a flat bilayer on a hydrophilic solid-liquid interface (*19*, *20*). Thus, a short linker consisting of two methylene groups was chosen. Besides, the relatively polar methacrylate groups in MA-11-2-11-MA were placed at the ends of the nonpolar alkyl tails to encourage the accumulation of methacrylate groups in the center of the bilayer. The high local concentration of methacrylate groups in the center of the bilayer favors their subsequent polymerization, providing an effective strategy to cross-link the MA-11-2-11-MA bilayer to form 2D networks.

To gain insight into the polymerization process and the 3D nanostructure of *net*-poly(MA-11-2-11-MA), we used DPD simulations to follow the structural evolution during polymerization. The coarse-grained model of MA-11-2-11-MA used in DPD contained two ammonium groups, two linear alkyl chains, and two methacrylate groups presented in blue, gray, and red beads, respectively (Fig. 2A). The initial model of the bilayer in an aqueous solution was constructed as two opposing monolayers of MA-11-2-11-MA, where the MA-11-2-11-MA molecules in each monolayer were vertically arranged with their methacrylate groups distributed randomly toward the middle of the bilayer. To match the bilayers of MA-11-2-11-MA in solution before the start of polymerization, we equilibrated the models in the initial period of the simulation. After the equilibration, the model maintained a bilayer structure (Fig. 2B). Five sublayers appeared in the bilayer: ammonium-alkyl-methacrylate-alkyl-ammonium. However, the bilayer of MA-11-2-11-MA was flexible, showing the uneven, rugged top and bottom surfaces. The regularity of each sublayer was relatively low, as indicated by the broad distribution for each component in the snapshot (Fig. 2B, left) and the density profiles (Fig. 2B, right). A small fraction of each component penetrated into the sublayers of other components. For instance, a close inspection of the snapshot reveals that some ammonium groups in the interior methacrylate sublayer and some methacrylate groups in the exterior ammonium sublayers. The density profile also reveals the permeation of water molecules deeply inside the hydrophobic alkyl-methacrylate-alkyl sublayers. This irregularity was mainly caused by thermal disturbance and a certain extent of miscibility among the components of MA-11-2-11-MA.

After the polymerization was switched on, the DPD simulation showed that the polymerization of MA-11-2-11-MA bilayer proceeded quickly, and the conversion of methacrylate groups reached a maximum of 98%. The rapid reaction rate and high conversion ratio can be attributed to the "condensation effect" of methacrylate groups, which is the high local concentration of methacrylate groups in the middle of the bilayer (*21*). It should be emphasized that the polymerization of gemini MA-11-2-11-MA can occur efficiently in such a dynamic bilayer environment, as indicated by a broad distribution of each component (Fig. 2B, right). The successful polymerization is a direct consequence of the dynamic self-adaptability of MA-11-2-11-MA, which allows the methacrylate groups to adjust their positions to fit the growth of polymer chains as the polymerization proceeds. Notably, the observed dynamic self-adaptability obviates the need to accurately align the polymerizable groups before or during polymerization, a substantial advantage compared to the use of crystalline monomers.

More intriguingly, a polymerization-induced self-organization effect was observed during the polymerization. Snapshots of the MA-11-2-11-MA bilayers at increasing conversion ratios of the methacrylate groups showed the regularity of each sublayer improving over time (Fig. 2C). This result indicates that the incompatibility between the methacrylate sublayer and the neighboring alkyl sublayers was magnified by polymerization.

At the completion of polymerization, a highly cross-linked bilayer of *net*-poly(MA-11-2-11-MA) was obtained (Fig. 2D). Compared to the structure of the unpolymerized MA-11-2-11-MA bilayer, the regularity of the polymeric bilayer improved substantially and the distribution of each component in the various sublayers was much narrower, as indicated by the snapshot (Fig. 2D, left) and the density profiles (Fig. 2D, right). The connected methacrylate groups in the poly(methacrylate) sublayer dragged the MA-11-2-11-MA molecules to a same plane, restraining the thermal disturbance of the MA-11-2-11-MA bilayer (Fig. 2D, left inset). In addition, the polymerization of methacrylate groups renders themselves to become immiscible in the adjacent sublayers, resulting in a spontaneous nanophase separation (*22*). This further enhanced the confinement of each component to its respective sublayer, leading to the formation of 2D *net*-poly(MA-11-2-11-MA) with well-defined sublayer structures and flat surfaces.

The structural evolution of MA-11-2-11-MA bilayer during the polymerization was fascinating, as interpreted above by the DPD simulation. To provide experimental support for this interpretation, we used ROESY, a powerful mean for molecular structure

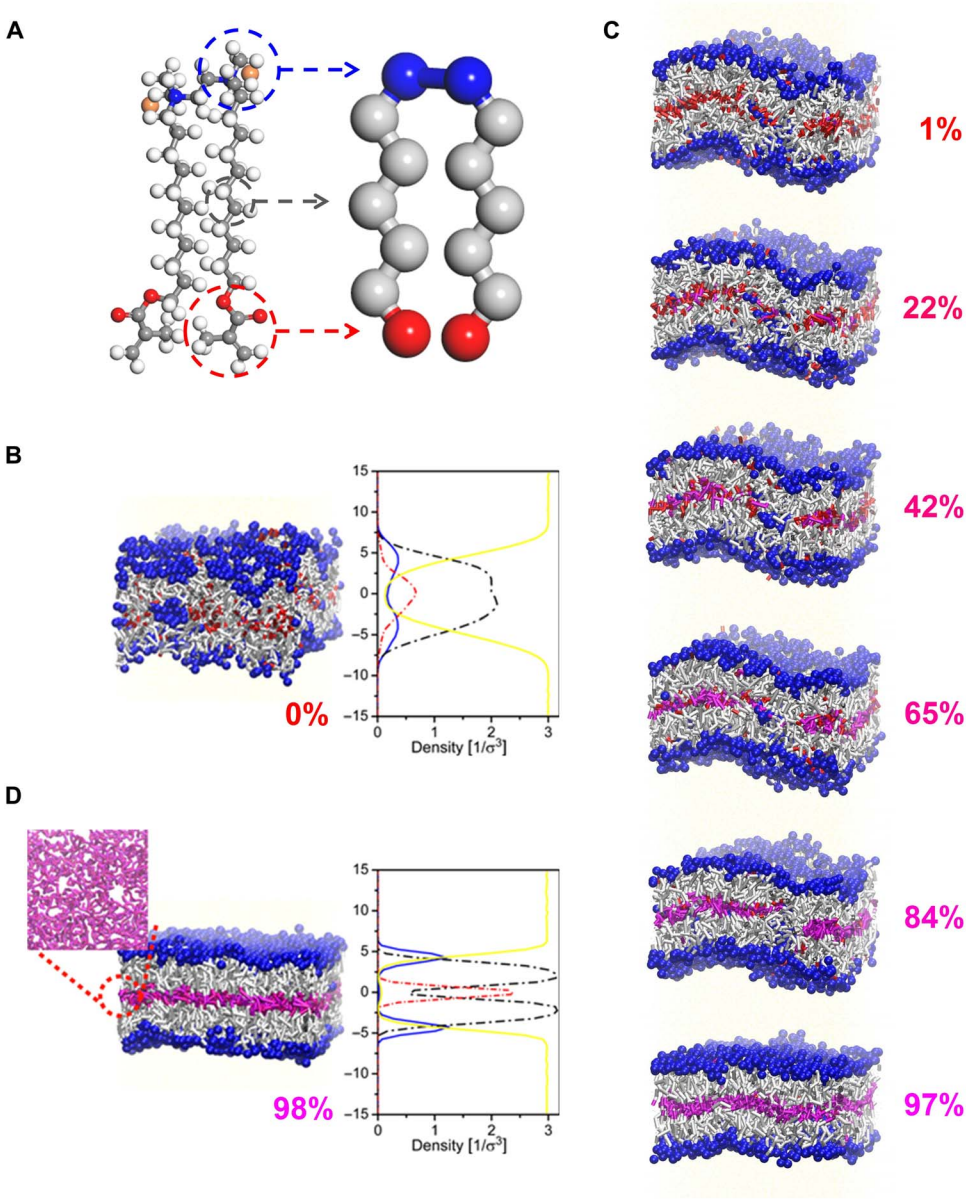

Fig. 2. DPD simulation of 2D *net*-poly(MA-11-2-11-MA). (**A**) Schematic illustration of the coarse-grained model of MA-11-2-11-MA. (**B**) Left: A representative snapshot of the MA-11-2-11-MA bilayer before polymerization. The conversion ratio of methacrylate groups is 0%. Right: Density profile of each component distributed in the vertical direction. Alkyl segments (black), ammonium groups (blue), methacrylate groups (red), and water (yellow). (**C**) Snapshots of MA-11-2-11-MA bilayers at increasing conversion ratios of methacrylate groups. (**D**) Left: A representative snapshot of the *net*-poly(MA-11-2-11-MA) bilayer after polymerization. The inset represents a top view of the poly(methacrylate) sublayer. The conversion ratio of the methacrylate groups is 98%. Right: Density profile of each component distributed in the vertical direction.

and conformation characterization, to investigate the arrangement of MA-11-2-11-MA molecules before and after the polymerization (Fig. 3 and fig. S6). In a ROESY spectrum, the coupling signals arise from protons in close proximity (5 Å), no matter whether the coupling were caused by intramolecular or intermolecular correlations (*23*). For MA-11-2-11-MA dissolved in dimethyl sulfoxide (DMSO) or in D_2O at a concentration below its CMC, MA-11-2-11-MA molecules were individually dispersed. When selectively irradiating the H-9 on the ammonium heads of MA-11-2-11-MA (as shown in Fig. 3A), only intramolecular coupling signals from protons, i.e., H-7, H-8, and H-10, near the ammonium heads were observed in the corresponding ROESY spectra (fig. S6). For MA-11-2-11-MA dissolved in D_2O at the concentration above its CMC, the intermolecular correlations arose as the MA-11-2-11-MA molecules were assembled into micelles of which the structure is similar to its bilayer on the substrates. Notably, the corresponding ROESY spectra by selectively irradiating H-9 show coupling signals from protons (H-1 to H-6) on the C_{11}-MA tails (Fig. 3B). These signals should be mainly assigned as intermolecular correlation between neighboring MA-11-2-11-MA molecules in the micelles. This result indicates that the ammonium heads

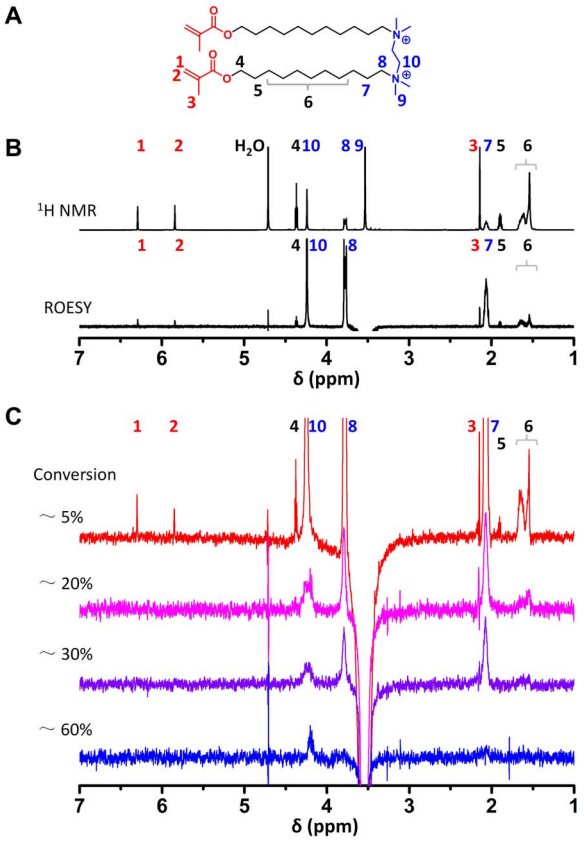

Fig. 3. NMR characterization of MA-11-2-11-MA assembly before and after polymerization. (**A**) Schematic illustration of the proton number in MA-11-2-11-MA. (**B**) ^{1}H NMR spectra of MA-11-2-11-MA assembly in D_2O at 65°C (top) and the corresponding ROESY spectra by the selective irradiation of proton H-9 (bottom). (**C**) ROESY spectra of MA-11-2-11-MA assembly by the selective irradiation of H-9 at increased conversion ratios of methacrylate groups. The conversion ratios were estimated from the FT-IR spectra.

and the C_{11}-MA tails had a wide spatial distribution in the micelles and that the micelle had a dynamic structure with limited regularity, which is consistent with the DPD simulation result for the bilayer structure before polymerization (Fig. 2B).

Subsequently, with the increase of the polymerization conversion ratio of methacrylate, the regularity of the MA-11-2-11-MA arrangement was gradually improved, as indicated by the ROESY spectra with selectively irradiation of H-9 (Fig. 3C). At a low conversion ratio of ca. 5% (the red line in Fig. 3C), all the coupling signals as the same as those before polymerization (Fig. 3B) were observed. When the conversion ratio increased to ca. 20% (the magenta line in Fig. 3C), the coupling signals of H-3 to H-6 were much weakened, and the signals of H-1 and H-2 completely disappeared. This result indicated that the intermolecular correlations between the ammonium heads and the C_{11}-MA tails of MA-11-2-11-MA decreased in the early stage of the polymerization. As the conversion ratio further increased to ca. 30%, (the violet line in Fig. 3C), the coupling signal of H-6 also disappeared, indicating the further improvement of arrangement regularity of MA-11-2-11-MA. Last, when the conversion ratio reached ca. 60% (the blue line in Fig. 3C), only coupling signals of H-10 remained. The disappearance of the ROESY signals between the protons on the C_{11}-MA tails and ammonium heads reveals the decrease in the distribution probability of these protons in close proximity and the improvement in the arrangement regularity of the MA-11-2-11-MA units during the polymerization process. This result agreed well with the polymerization-induced self-organization effect of MA-11-2-11-MA bilayers interpreted by the DPD simulation.

To explore the possibility of preparing 2D copolymers, we also simulated the polymerization scenario where the bilayer was randomly doped with 10% (molar ratio) of monomeric MA-11-Me_3. Copolymerization of MA-11-2-11-MA and MA-11-Me_3 also yielded a highly cross-linked 2D copolymer *net*-poly(MA-11-2-11-MA)-*co*-(MA-11-Me_3), and a similar polymerization-induced self-organization effect was also observed (fig. S7). In the simulation for the *net*-poly(MA-11-2-11-MA)-*co*-(MA-11-Me_3), the regularity of each sublayer in the binary bilayer also gradually improved with increasing conversion. The conversion of methacrylate groups reached 99% for the copolymerization, which demonstrated a potentially viable strategy to functionalized 2DSPs via copolymerization of MA-11-2-11-MA with its functional derivatives.

Functionalization of 2D *net*-poly(MA-11-2-11-MA)

Despite the progress made to date toward 2DSPs, effective functionalization of 2DSPs remains a formidable challenge with a highly rewarding solution due to the range of properties anticipated in these polymers (*24*, *25*). The observed self-adaptability of gemini MA-11-2-11-MA during polymerizations makes it an excellent precursor to functionalized 2DSPs, where 2DSPs with tunable properties can be synthesized with varying functional groups by copolymerization.

We explored a simple route to functionalized 2DSPs by incorporating a wide range of monomeric derivatives of MA-11-2-11-MA. Compared to gemini MA-11-2-11-MA, the monomeric derivatives (MA-11-F) have a polymerizable methacrylate group (MA), a hydrophobic alkyl chain with an identical length (C_{11}), and an ammonium head group carrying desired functional groups (F) (Fig. 4A). This structural resemblance facilitates the coassembly of MA-11-F with MA-11-2-11-MA to form a binary bilayer that can be polymerized to yield functionalized 2D *net*-poly(MA-11-2-11-MA)-*co*-(MA-11-F). For example, we introduced fluorescent moieties rhodamine B (RhB), fluorescein (Fls), and pyrene (Pyr) in the monomeric derivatives, whose fluorescence emissions are in red, green, and blue, respectively (Fig. 4A). These fluorescent monomeric derivatives were copolymerized with MA-11-2-11-MA at a molar fraction of 10% on separate silicon substrates, yielding 2D copolymer films of *net*-poly(MA-11-2-11-MA)-*co*-(MA-11-F) (F = RhB, Fls, or Pyr) with red, green, and blue fluorescence. The films were then patterned to letter shapes using oxygen RIE (Fig. 4B). We characterized two samples of the fluorescent films (i.e., the edge of the "2" and the "l" in Fig. 4B) with AFM. Both the roughness and the thickness of the copolymer film were consistent with those of the 2D *net*-poly(MA-11-2-11-MA) film shown in Fig. 1B (fig. S8, A and B). In contrast, the edges of the 2 and the l were indented from the roughness of the mask fabricated by laser beam lithography. The successful patterning of *net*-poly(MA-11-2-11-MA)-*co*-(MA-11-F) confirms its use as a positive resist for lithography with nanometer resolution.

Next, we explored an alternative strategy to functionalized 2DSPs of *net*-poly(MA-11-2-11-MA) via post-polymerization reactions. First, we demonstrate that a variety of reactive groups can be introduced onto the ammonium head group of the monomeric derivatives, such as a hydroxyl group (in MA-11-OH) and a carboxyl group (in MA-11-COOH) for esterification reactions, as well as an

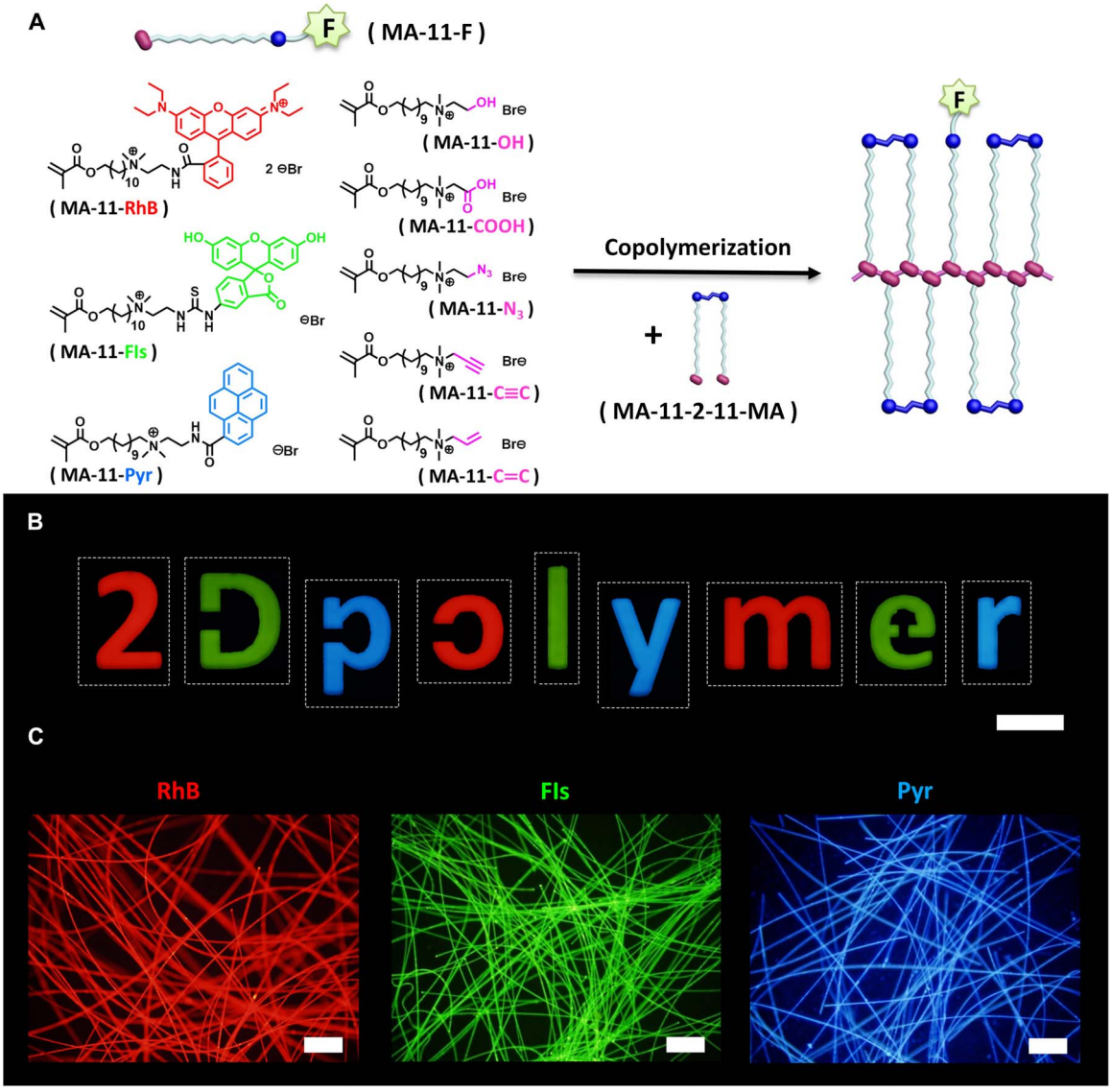

Fig. 4. Functionalization of 2D *net*-poly(MA-11-2-11-MA). (**A**) Chemical structures of the monomeric derivatives (MA-11-F; F, various functional groups) and copolymerization with MA-11-2-11-MA. (**B**) Fluorescence films of *net*-poly(MA-11-2-11-MA)-*co*-(MA-11-F) (F = RhB, Fls, or Pyr) in number and letter shapes (scale bar, 500 μm). (**C**) Fluorescence microscope images of *net*-poly(MA-11-2-11-MA)-*co*-(MA-11-C≡C)–coated silica wool after post-polymerization functionalization with RhB-EO_4-N_3, Fls-EO_4-N_3, and Pyr-EO_4-N_3 via click reactions (scale bars, 200 μm).

azido group (in MA-11-N_3), an acetylene group (in MA-11-C≡C), and a propylene group (in MA-11-C=C) for click reactions. These groups provide reaction sites that remain accessible after copolymerization and allows the elaboration of *net*-poly(MA-11-2-11-MA)-*co*-(MA-11-F) by reaction with functional molecules. Characterization of the 2D copolymers by infrared spectroscopy confirmed the successful introduction of the desired reactive groups into *net*-poly(MA-11-2-11-MA)-*co*-(MA-11-F) (F = OH, COOH, N_3, C≡C, and C=C) after copolymerization (fig. S8C). We subsequently performed post-polymerization functionalization of *net*-poly(MA-11-2-11-MA)-*co*-(MA-11-C≡C) by grafting the 2DSP onto the surface of silica wool (diameter of 5 μm and length of 2 to 5 cm). After polymerization, RhB-EO_4-N_3, Fls-EO_4-N_3, and Pyr-EO_4-N_3 were linked to *net*-poly(MA-11-2-11-MA)-*co*-(MA-11-C≡C) on the surface of silica wool via click reactions (*26*). The vivid fluorescence of the silica wool in fluorescence microscopy (Fig. 4C) confirmed the functionalization of *net*-poly(MA-11-2-11-MA)-*co*-(MA-11-C≡C)–coated silica wool with RhB, Fls, and Pyr.

Microstructures of 2D *net*-poly(MA-11-2-11-MA)

2DSPs with an identical chemical composition but different microstructures may present additional and intriguing properties suitable for a wide range of potential applications, such as drug delivery, microreactors, biomimetic sensors, and superhydrophobic surfaces (*27*). However, 2DSPs produced from single crystals or Langmuir-Blodgett films in previous research lacked variety in shapes (*4*–*6*). The self-adaptability of gemini MA-11-2-11-MA observed during polymerization should make it a versatile monomer that can be polymerized

into 2D *net*-poly(MA-11-2-11-MA) with various microstructures, using microscale particles as templates. As a proof of principle, MA-11-2-11-MA was copolymerized with MA-11-RhB as a colorant (10% molar ratio) on a series of silica particles, such as microspheres, microrods, and microboards (insets in Fig. 5, A to C). The microspheres had average diameters of 1.0 μm, the microrods had average dimensions of 2.0 μm by 0.3 μm, and the microboards had average dimensions of 4.2 μm by 0.8 μm by 0.1 μm. The resulting 2D *net*-poly(MA-11-2-11-MA)-*co*-(MA-11-RhB) formed a uniform layer over the entire surface of the silica particles, as indicated by the bright fluorescence throughout all particles in fluorescent microscopy images (insets in Fig. 5, D to F).

To create hollow polymeric structures, we removed the silica particle templates by etching with hydrofluoric acid. Capsules of *net*-poly(MA-11-2-11-MA)-*co*-(MA-11-RhB) with well-preserved structures were obtained, which retained the dimensions of the silica templates (TEM images in Fig. 5, A to C; fluorescence microscopy images in Fig. 5, D to F). The series of polymerization and etching experiments further confirm that 2D copolymers of *net*-poly(MA-11-2-11-MA)-*co*-(MA-11-RhB) can form a highly cross-linked network with sufficient mechanical strength to maintain its structural integrity in hollow structures with a variety of shapes. One side of the silica microrods has more porous structure (Fig. 5B, inset, and fig. S9B), leading to a higher incorporation density of the 2D copolymer. The resulting capsules on the porous side showed a deeper contrast in TEM images (Fig. 5B and fig. S9C) and brighter fluorescence in fluorescence microscope images (Fig. 5E). These promising results indicate that the template-directed polymerization of gemini MA-11-2-11-MA is not limited to microparticles with large convex surfaces but is also possible on nanoscale concave surfaces.

Surface modifier and antibacterial properties

Surface modification is a crucial method for conferring additional functionalities to objects and interfaces. Encouraged by the successful polymerization of gemini MA-11-2-11-MA on various microstructures, we explored the feasibility of its polymerization on macroscale objects. Representative materials composed of inorganic oxide (quartz cuvette), metal (copper coin), and polymer (petri dish of sulfonated polystyrene) were selected as substrates. We deliberately chose objects with negatively charged surfaces to enhance the adsorption of positively charged MA-11-2-11-MA and MA-11-RhB (*28–30*). Subsequent copolymerization using standard conditions yielded an extremely pale pink film that uniformly covered the entire surface of these macroscale objects (Fig. 6A, top series). The fluorescence images confirmed the successful formation of 2D *net*-poly(MA-11-2-11-MA)-*co*-(MA-11-RhB) over a large area on a variety of surfaces (Fig. 6A, bottom series). These results point to the feasibility of the preparation of 2D-*net*-poly(MA-11-2-11-MA)-*co*-(MA-11-RhB) on macroscale surfaces of various composition and its ability to act as a surface modifier.

Quaternary ammonium–based cationic polyelectrolytes have been extensively studied for their excellent antimicrobial properties (*31*). As an extension to this work, we showed that gemini MA-11-2-11-MA can be polymerized on cotton gauze to form a robust network of polycations with desirable antimicrobial properties for biomedical applications. Using standard conditions, positively charged MA-11-2-11-MA and MA-11-RhB were copolymerized onto a piece of cotton gauze, and the gauze was then thoroughly washed with DI water. The pink color of RhB groups on the gauze that was modified with the fluorescent copolymer *net*-poly(MA-11-2-11-MA)-*co*-(MA-11-RhB) was well preserved after washing (Fig. 6B, right).

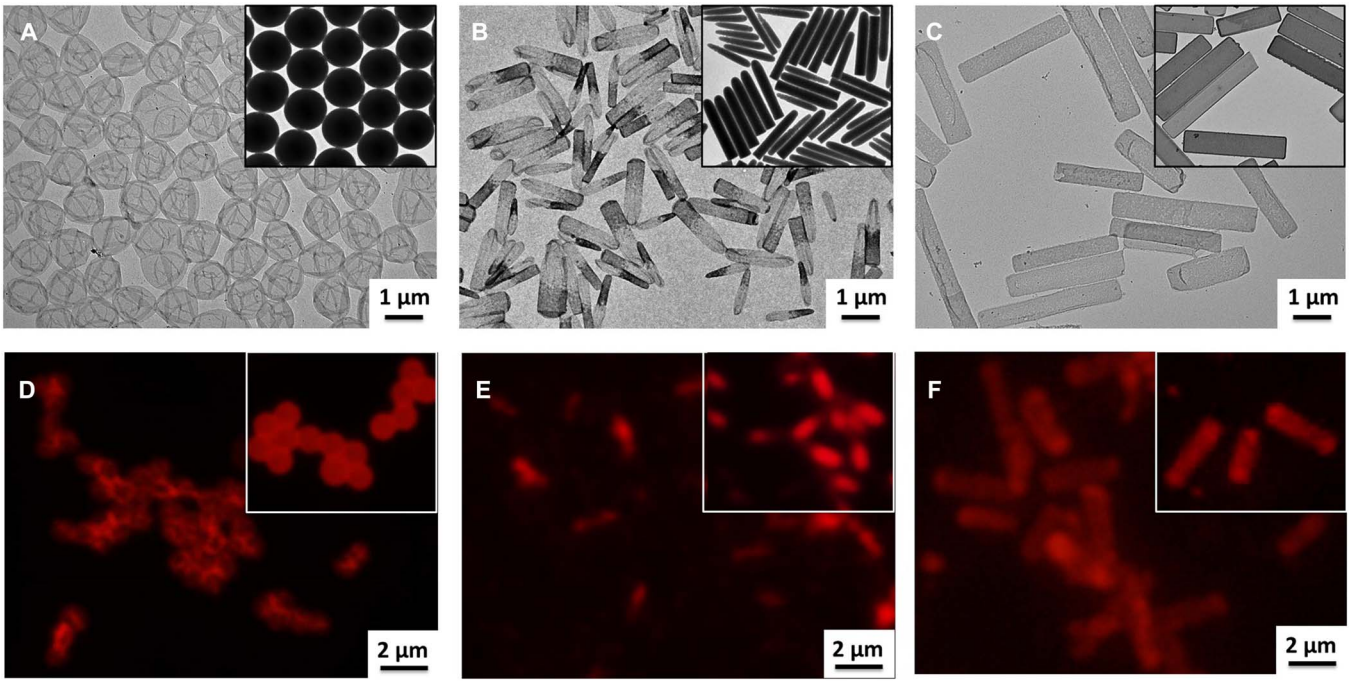

Fig. 5. Microstructures of 2D *net*-poly(MA-11-2-11-MA)-*co*-(MA-11-RhB). (**A** to **C**) TEM images of *net*-poly(MA-11-2-11-MA)-*co*-(MA-11-RhB)–coated silica microspheres, microrods, microboards (insets), and the corresponding hollow capsules. (**D** to **F**) Fluorescence microscopy images of *net*-poly(MA-11-2-11-MA)-*co*-(MA-11-RhB)–coated silica microspheres, microrods, microboards (insets), and the corresponding hollow capsules.

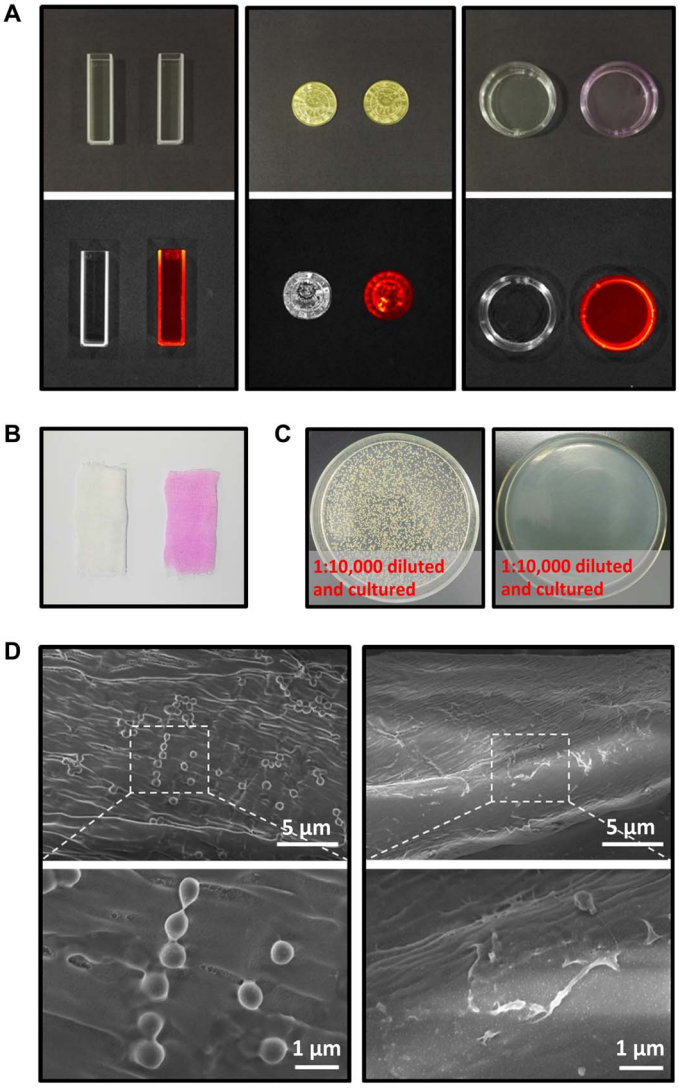

Fig. 6. Surface modification and antibacterial property of 2D copolymers. (**A**) Quartz cuvettes, copper coins, and sulfonated polystyrene petri dishes before (left) and after (right) coating with fluorescent *net*-poly(MA-11-2-11-MA)-*co*-(MA-11-RhB). Images in the top series are photographs, and those in the bottom series are the corresponding fluorescence images. (Photo Credit: Yang Li, Jilin University). (**B**) Cotton gauze before (left) and after coating with fluorescent *net*-poly(MA-11-2-11-MA)-*co*-(MA-11-RhB) and thoroughly washing (right) (Photo Credit: Yang Li, Jilin University). (**C**) Proliferation of *S. aureus* released from the cotton gauze without (left) and with (right) *net*-poly(MA-11-2-11-MA)-*co*-(MA-11-RhB) (Photo Credit: Yang Li, Jilin University). (**D**) SEM images of *S. aureus* on the cotton gauze without (left) and with (right) *net*-poly(MA-11-2-11-MA)-*co*-(MA-11-RhB).

Subsequently, the antibacterial properties of the copolymer-coated gauze were tested with *Staphylococcus aureus* with untreated gauze serving as a control. The proliferation of *S. aureus* from the *net*-poly(MA-11-2-11-MA)-*co*-(MA-11-RhB)–coated gauze (Fig. 6C, right) was substantially reduced compared to that of the untreated gauze (Fig. 6C, left). Scanning electron microscopy (SEM) analysis revealed intact cells of *S. aureus* on the untreated gauze (Fig. 6D, left), while only residues of dead cells were found on coated gauze (Fig. 6D, right). These results convincingly demonstrate that cationic *net*-poly(MA-11-2-11-MA)-*co*-(MA-11-RhB) on the gauze effectively destroyed the membrane of *S. aureus*.

DISCUSSION

In this work, we demonstrate that the polymerization of gemini MA-11-2-11-MA on solid-liquid interfaces is a powerful synthetic strategy that allows unprecedented access to a wide range of 2DSPs with well-controlled size and shape and functionalities. The careful design of the gemini monomer imparts it with dynamic self-adaptability, a critical factor in the efficient packing of MA-11-2-11-MA in a bilayer and the resulting very high conversions in homo- and copolymerizations. This dynamic self-adaptability also ensures a high degree of compatibility between MA-11-2-11-MA and monomeric derivatives carrying diverse functional groups (i.e., MA-11-F), permitting the synthesis of 2D copolymer *net*-poly(MA-11-2-11-MA)-*co*-(MA-11-F) in just one step. A second consequence of the rational design of MA-11-2-11-MA is the self-organization effect during polymerization, leading to the formation of highly cross-linked, single-bilayer-thick 2D *net*-poly(MA-11-2-11-MA) with outstanding mechanical strength. This allows the polymerization of gemini MA-11-2-11-MA on multiple types of solid substrates with varying surface curvatures and dimensions. Subsequent removal of the templates yields hollow, freestanding capsules of 2D *net*-poly(MA-11-2-11-MA), whose structural integrity is a testament to the mechanical strength of the 2DSPs. The exceptional versatility of 2D *net*-poly(MA-11-2-11-MA)-*co*-(MA-11-F) allows its use as a positive resist with nanoscale precision in oxygen RIE and as a superb antibacterial agent against *S. aureus*. These preliminary experiments support our interfacial polymerization strategy as a highly promising route to candidates for future applications such as biomimetic sensors, separation membranes, drug delivery vehicles, and structural reinforcement agents.

As the preparation of 2DSP via gemini monomer bilayers sidesteps the synthetic challenge associated with crystalline monomers, our strategy of polymerization at the solid-liquid interface is anticipated to be compatible with a much broader range of monomers compared to topochemical solid-state polymerization. This is a substantial advance in the field of 2DSPs, as the design and synthesis of monomers will no longer be the rate-limiting step of the overall process. On the other hand, for this advance to cause a leap in the field of 2DSPs, one has to be able to compensate the criterion of "periodicity" (i.e., crystallinity) in the definition of 2D polymers previously proposed by Schlüter and co-workers (*4*–*6*, *13*). Periodicity is the essential feature of crystals, but it is not essential for polymers. In general, polymers are amorphous (i.e., glassy) or semicrystalline, regardless of whether they are 1D or 3D polymers. A defining criterion that focuses on the periodicity (i.e., crystallinity) might impede the development of 2D polymers, and more investigation is needed to decide whether 2D polymers must be "periodic" (i.e., crystalline).

In summary, this research broadens the synthetic methods for 2DSPs and brings them into the realm of easy access for practical applications. We predict that this will become an important milestone in the development of 2DSPs, eventually affording them the same diverse range of structural features, uses, and applications, as observed for their 1D counterparts.

MATERIALS AND METHODS

Materials

11-Bromo-1-undecanol (98%), methacryloyl chloride (96%), 4-methoxyphenol (98%), *N*,*N*,*N*′,*N*′-tetramethylethylenediamine (98%), *N*,*N*-dimethylethanolamine (98%), *N*,*N*-dimethylglycine sodium (98%), 2-dimethylaminoethyl chloride hydrochloride (98%),

N,*N*-dimethylpropargylamine (98%), *N*,*N*-dimethylallylamine (98%), RhB (95%), fluorescein isothiocyanate (FITC, 95%), 1-pyrenecarboxylic acid (97%), *N*,*N*-dimethylethylenediamine (98%), 11-azido-3,6,9-trioxaundecan-1-amine (NH_2-EG_4-N_3, 98%), 1-(3-dimethylaminopropyl)-3-ethylcarbodiimide hydrochloride (EDCI, 96%), 4-dimethylaminopyridine (DMAP, 98%), ACVA (97%), tetraethyl orthosilicate (>99%), and ammonium hydroxide solution [28 weight % (wt %)] were purchased from Sigma-Aldrich and used as received. Silica microspheres (1.0 μm) were purchased from New Mater Nanotechnology. Solvents such as tetrahydrofuran (THF), ethyl ether, acetonitrile, DMSO, dichloromethane (DCM), anhydrous ethanol, and methanol (analytical grade) were purchased from Beijing Chemical Works. DI water (18.2 megohms) was used in all the experiments.

Characterizations

AFM characterization was carried out in soft tapping mode in air on Bruker Dimension FastScan. TEM images were obtained on a Hitachi H-800 instrument at 175 kV. The silica microparticles were dropped on a carbon-coated TEM grid and dried in air. XPS measurement was performed by using a PREVAC XPS/UPS System. FT-IR spectra were recorded on a Bruker VERTEX 80v spectrometer. All spectra were collected at an accumulation of 32 scans with 4-cm^{-1} resolution. The proton nuclear magnetic resonance (^{1}H NMR) spectra were recorded at 500 MHz on a Bruker AVANCE 500 spectrometer at room temperature.

Synthesis of MA-11-2-11-MA

MA-11-2-11-MA was synthesized through a two-step method. First, 11-bromoundecyl methacrylate was synthesized according to the previous report (*32*). Next, 11-bromoundecyl methacrylate (1.43 g, 4.5 mmol), *N*,*N*,*N*′,*N*′-tetramethylethylenediamine (174 mg, 1.5 mmol), and 4-methoxyphenol (trace) were dissolved in 20-ml mixed solvents (acetonitrile:water = 19:1 by volume) under nitrogen atmosphere. After reaction at 80°C for 48 hours, the solvent was evaporated off, and the obtained residue was washed with THF to remove excess reactants and single substituted product. Further purification was carried out by recrystallization in water. MA-11-2-11-MA was obtained as a white solid with a yield of 80%.

^{1}H NMR (500 MHz, $CDCl_3$): δ [parts per million (ppm)] 6.09 (s, 2H, CH_2=C), 5.56 (s, 2H, CH_2=C), 4.80 (s, 4H, N—CH_2—CH_2—N), 4.13 (t, 4H, —CH_2—OOC), 3.72 (t, 4H, N—CH_2—), 3.52 (s, 12H, N—CH_3), 1.94 (s, 6H, CH_3—C=C), 1.81 (m, 4H, —CH_2—CH_2—OOC), 1.67 (m, 4H, —CH_2—CH_2—N), and 1.24 to 1.44 [m, 28H, —$(CH_2)_7$—]. Matrix-assisted laser desorption/ionization–time-of-flight (MALDI-TOF) (positive ion): Calculated mass/charge ratio (Calcd *m*/*z*) for $C_{36}H_{70}O_4N_2^{2+}$: 297.27; found, 297.29. Elemental analysis: Calcd % for $C_{36}H_{70}O_4N_2Br_2$: C, 57.29; H, 9.35; N, 3.71; found, C, 57.05; H, 9.33; N, 3.96.

Synthesis of MA-11-OH

11-Bromoundecyl methacrylate (0.32 g, 1.0 mmol), *N*,*N*-dimethylethanolamine (1.0 ml, 10 mmol), and 4-methoxyphenol (trace) were dissolved in 9.0-ml THF under nitrogen atmosphere. After reaction at 60°C for 15 hours, the solvent was evaporated off, and the obtained crude product was washed with diethyl ether to remove the impurities. MA-11-OH was obtained as a white solid with a yield of 88%.

^{1}H NMR (500 MHz, $CDCl_3$): δ (ppm) 6.09 (s, 1H, CH_2=C), 5.55 (s, 1H, CH_2=C), 4.16 (t, 2H, —CH_2—OH), 4.14 (t, 2H, —CH_2—OOC), 3.75 (t, 2H, N—CH_2—CH_2OH), 3.54 (t, 2H, N—CH_2—), 3.38 (s, 6H, N—CH_3), 1.94 (s, 3H, CH_3—C=C), 1.76 (m, 2H, —CH_2—CH_2—OOC), 1.67 (m, 2H, —CH_2—CH_2—N), and 1.24 to 1.44 [m, 14H, —$(CH_2)_7$—]. MALDI-TOF (positive ion): Calcd *m*/*z* for $C_{19}H_{38}O_3N_1^+$: 328.28; found, 328.29.

Synthesis of MA-11-COOH

11-Bromoundecyl methacrylate (0.32 g, 1.0 mmol), *N*,*N*-dimethylglycine sodium (0.20 g, 2.1 mmol), and 4-methoxyphenol (trace) were dissolved in 10-ml methanol under nitrogen atmosphere. After reaction at 60°C for 20 hours, the solvent was evaporated off under reduced pressure, and the obtained solid was washed with diethyl ether. The crude product was eluted with chloroform and dried by evaporation. MA-11-COOH was obtained as a milk-white solid with a yield of 44%.

^{1}H NMR (500 MHz, $CDCl_3$): δ (ppm) 6.09 (s, 1H, CH_2=C), 5.56 (s, 1H, CH_2=C), 4.32 (s, 2H, N—CH_2—C=O), 4.13 (t, 2H, —CH_2—OOC), 3.63 (t, 2H, N—CH_2—), 3.35 (s, 6H, N—CH_3), 1.94 (s, 3H, CH_3—C=C), 1.76 (m, 2H, —CH_2—CH_2—OOC), 1.67 (m, 2H, —CH_2—CH_2—N), and 1.24 to 1.44 [m, 14H, —$(CH_2)_7$—]. MALDI-TOF (positive ion): Calcd *m*/*z* for $C_{19}H_{36}O_4N_1^+$: 342.26; found, 342.27.

Synthesis of MA-11-N_3

MA-11-N_3 was synthesized through a two-step method. First, NaN_3 (0.67 g, 10 mmol) and 2-dimethylaminoethyl chloride hydrochloride (0.72 g, 5.0 mmol) were dissolved in 25 ml of DI water under nitrogen atmosphere. After reaction at 60°C for 15 hours, NaOH (0.20 g, 5.0 mmol) was added, and the solution was extracted with diethyl ether three times. The organic layer was collected, and the solvent was evaporated off slowly to avoid the loss of product. 2-Azido-*N*,*N*-dimethylethanamine was obtained as a light yellow liquid with a yield of 52%.

^{1}H NMR (500 MHz, $CDCl_3$): δ (ppm) 3.39 (t, 2H, —CH_2—N_3), 2.54 (t, 2H, —CH_2—N), and 2.31 (6H, CH_3—N).

Next, 11-bromoundecyl methacrylate (0.32 g, 1.0 mmol), 2-azido-*N*,*N*-dimethylethanamine (0.29 g, 2.5 mmol), and 4-methoxyphenol (trace) were dissolved in 10-ml THF under nitrogen atmosphere. After reaction at 60°C for 15 hours, the solvent was evaporated off, and the obtained crude product was washed with diethyl ether to remove the impurities. MA-11-N_3 was obtained as a white solid with a yield of 37%.

^{1}H NMR (500 MHz, $CDCl_3$): δ (ppm) 6.09 (s, 1H, CH_2=C), 5.56 (s, 1H, CH_2=C), 4.13 (t, 2H, —CH_2—OOC), 3.70 (t, 2H, N—CH_2—CH_2—N_3), 3.54 (t, 2H, N—CH_2—), 3.42 (t, 2H, N—CH_2—CH_2—N_3), 3.38 (s, 6H, N—CH_3), 1.94 (s, 3H, CH_3—C=C), 1.76 (m, 2H, —CH_2—CH_2—OOC), 1.67 (m, 2H, —CH_2—CH_2—N), and 1.24 to 1.44 [m, 14H, —$(CH_2)_7$—]. MALDI-TOF (positive ion): Calcd *m*/*z* for $C_{19}H_{37}O_2N_4^+$: 353.29; found, 353.31.

Synthesis of MA-11-C≡C

11-Bromoundecyl methacrylate (0.32 g, 1.0 mmol), *N*,*N*-dimethylpropargylamine (2.0 ml, 18.6 mmol), and 4-methoxyphenol (trace) were dissolved in 8.0-ml THF under nitrogen atmosphere. After reaction at 60°C for 20 hours, the solvent was evaporated off, and the obtained crude product was washed with diethyl ether to remove the impurities. MA-11-C≡C was obtained as a white solid with a yield of 73%.

^{1}H NMR (500 MHz, $CDCl_3$): δ (ppm) 6.09 (s, 1H, CH_2=C), 5.55 (s, 1H, CH_2=C), 4.86 (s, 2H, N—CH_2—C≡C), 4.14 (t, 2H, —CH_2—OOC), 3.65 (t, 2H, —CH_2—N), 3.51 (s, 6H, CH_3—N), 2.85 (s, 1H, C≡CH), 1.94 (s, 3H, CH_3—C=C), 1.76 (m, 2H,

—CH_2—CH_2—OOC), 1.67 (m, 2H, —CH_2—CH_2—N), and 1.24 to 1.44 [m, 14H, —$(CH_2)_7$—]. MALDI-TOF (positive ion): Calcd *m*/*z* for $C_{20}H_{36}O_2N_1^+$: 322.27; found, 322.28.

Synthesis of MA-11-C=C

11-Bromoundecyl methacrylate (0.32 g, 1.0 mmol), *N*,*N*-dimethylallylamine (2.0 ml, 16.9 mmol), and 4-methoxyphenol (trace) were dissolved in 8.0-ml THF under nitrogen atmosphere. After reaction at 60°C for 20 hours, the solvent was evaporated off, and the obtained crude product was washed with diethyl ether to remove the impurities. MA-11-C=C was obtained as a white solid with a yield of 63%.

^{1}H NMR (500 MHz, $CDCl_3$): δ (ppm) 6.09 [s, 1H, CH_2=C(CH_3)], 5.97 (m, 1H, CH_2-*CH*=CH_2), 5.88 (d, 1H, CH_2—CH=CH_2), 5.77 (d, 1H, CH_2—CH=CH_2), 5.55 [s, 1H, CH_2=C(CH_3)], 4.36 (d, 2H, N—CH_2-CH=CH_2), 4.14 (t, 2H, —CH_2-OOC), 3.49 (t, 2H, —CH_2—N), 3.37 (s, 6H, N—CH_3), 1.94 (s, 3H, CH_3—C=C), 1.76 (m, 2H, —CH_2—CH_2—OOC), 1.67 (m, 2H, —CH_2—CH_2—N), and 1.24 to 1.44 [m, 14H, —$(CH_2)_7$—]. MALDI-TOF (positive ion): Calcd *m*/*z* for $C_{20}H_{38}O_2N_1^+$: 324.29; found, 324.31.

Synthesis of MA-11-RhB

MA-11-RhB was synthesized through a two-step method. First, RhB (0.48 g, 1.0 mmol) and EDCI (0.23 g, 1.2 mmol) were dissolved in 30-ml anhydrous DCM under the ice bath and stirred for 10 min. Then, *N*,*N*-dimethylethylenediamine (0.50 ml, 4.6 mmol) and DMAP (6.11 mg, 0.05 mmol) were added. The solution was allowed to slowly rise to room temperature and reacted overnight in the dark. After that, the solution was concentrated, and the product was purified by column chromatography.

^{1}H NMR (500 MHz, $CDCl_3$): δ (ppm) 8.28 (d, 1H, Ph), 7.84 (t, 1H, Ph), 7.76 (t, 1H, Ph), 7.34 (d, 1H, Ph), 7.08 (d, 2H, Ph), 6.97 (d, 2H, Ph), 6.84 (s, 2H, Ph), 3.66 (m, 2H CONH—CH_2—CH_2—N; 8H, CH_3—CH_2—N), 2.55 (t, 2H, CONH—CH_2—CH_2—N), 2.24 (s, 6H, N—CH_3), and 1.34 (t, 12H, CH_3—CH_2—N).

Next, above product (0.27 g, 0.50 mmol), 11-bromoundecyl methacrylate (0.16 g, 0.50 mmol) and 4-methoxyphenol (trace) were dissolved in 10-ml acetonitrile under nitrogen atmosphere. After reaction at 60°C for 24 hours in the dark, the solvent was evaporated off, and the crude product was washed with THF to remove the impurities. MA-11-RhB was obtained as a reddish-brown solid with a yield of 38%.

^{1}H NMR (500 MHz, $CDCl_3$): δ (ppm) 8.28 (d, 1H, Ph), 7.82 (t, 1H, Ph), 7.74 (t, 1H, Ph), 7.33 (d, 1H, Ph), 7.07 (d, 2H, Ph), 6.90 (d, 2H, Ph), 6.84 (s, 2H, Ph), 6.09 (s, 1H, CH_2=C), 5.54 (s, 1H, CH_2=C), 4.13 (t, 2H, —CH_2—OOC), 4.01 (t, 2H, CONH—CH_2—CH_2—N), 3.72 (t, 2H, CONH—CH_2—CH_2—N), 3.52 (t, 2H, CH_2—CH_2—N), 3.66 (m, 8H, CH_3—CH_2—N), 3.37 (s, 6H, N—CH_3), 1.94 (s, 3H, CH_3—C=C), 1.76 (m, 2H, —CH_2—CH_2—OOC), 1.66 (m, 2H, —CH_2—CH_2—N), and 1.10 to 1.40 [m, 12H + 14H, CH_3—CH_2—N + —$(CH_2)_7$—].

Synthesis of MA-11-Fls

MA-11-Fls was synthesized through a two-step method. FITC (0.39 g, 1.0 mmol) was dissolved in 20-ml anhydrous DCM under the ice bath, and *N*,*N*-dimethylethylenediamine (0.50 ml, 4.6 mmol) was added. The solution was allowed to slowly rise to room temperature and reacted overnight in the dark. Then, the solution was concentrated and deposited in diethyl ether three times to remove the impurities.

^{1}H NMR (500 MHz, DMSO): δ (ppm) 8.35 (s, 1H, Ph), 7.76 (d, 1H, Ph), 7.17 (d, 1H, Ph), 6.67 (s, 2H, Ph), 6.57 (m, 4H, Ph), 3.59 (s, 2H, N—CH_2—CH_2—NHSC), 2.40 (s, 2H, N—CH_2—CH_2—NHSC), 2.21 (s, 6H, N—CH_3), and 10.22 and 8.00 (—OH and —NH—, position and integral variable).

Next, above product (0.24 g, 0.5 mmol), 11-bromoundecyl methacrylate (0.16 g, 0.5 mmol) and 4-methoxyphenol (trace) were dissolved in 2-ml DMSO under nitrogen atmosphere. After reaction at 45°C for 24 hours in the dark, the solution was deposited into a mixed solvent (diethyl ether:THF = 5:1 by volume) three times to remove the impurities. MA-11-Fls was obtained as a brown-yellow solid with a yield of 32%.

^{1}H NMR (500 MHz, DMSO): δ (ppm) 8.23 (s, 1H, Ph), 7.74 (d, 1H, Ph), 7.22 (d, 1H, Ph), 6.68 (s, 2H, Ph), 6.57 (m, 4H, Ph), 6.00 (s, 1H, CH_2=C), 5.66 (s, 1H, CH_2=C), 4.07 (t, 2H, —CH_2—OOC), 3.75 (t, 2H, CSNH—CH_2—CH_2—N), 3.52 (m, 2H, CH_2—CH_2—N; 2H, CSNH—CH_2—CH_2—N), 3.12 (s, 6H, N-CH_3), 1.87 (s, 3H, CH_3—C=C), 1.72 (m, 2H, —CH_2—CH_2—OOC), 1.59 (m, 2H, —CH_2—CH_2—N), and 1.20 to 1.35 [m, 14H, —$(CH_2)_7$—]. MALDI-TOF (positive ion): Calcd *m*/*z* for $C_{40}H_{50}O_7N_3S^+$: 716.34; found, 716.28.

Synthesis of MA-11-Pyr

MA-12-Pyr was synthesized through a two-step method. 1-Pyrenecarboxylic acid (0.50 g, 2.0 mmol) and EDCI (0.46 g, 2.4 mmol) were dissolved in 40-ml anhydrous DCM under the ice bath and stirred for 10 min. *N*,*N*-Dimethylethylenediamine (1.0 ml, 9.2 mmol) and DMAP (12.2 mg, 0.1 mmol) were added. The solution was allowed to slowly rise to room temperature and reacted 24 hours in the dark. After that, the solution was concentrated, and the product was purified by column chromatography.

^{1}H NMR (500 MHz, $CDCl_3$): δ (ppm) 9.27 (s, 1H, Ph), 8.67 (s, 1H, Ph), 8.30 to 8.05 (m, 7H, Ph), 3.64 (t, 2H, CONH—CH_2—CH_2—N), 2.50 (t, 2H, CONH—CH_2—CH_2—N), and 2.28 (s, 6H, N—CH_3).

Next, above product (0.16 g, 0.50 mmol), 11-bromoundecyl methacrylate (0.16 g, 0.50 mmol) and 4-methoxyphenol (trace) were dissolved in 10-ml acetonitrile under nitrogen atmosphere. After reaction at 60°C for 24 hours in the dark, the solvent was evaporated off, and the crude product was washed with diethyl ether to remove the impurities. MA-11-Pyr was obtained as a pea green solid with a yield of 57%.

^{1}H NMR (500 MHz, $CDCl_3$): δ (ppm) 9.26 (s, 1H, Ph), 8.66 (s, 1H, Ph), 8.31 to 8.01 (m, 7H, Ph), 6.09 (s, 1H, CH_2=C), 5.55 (s, 1H, CH_2=C), 4.50 (t, 2H, N—CH2—CH_2—NHOC), 4.15 (t, 2H, —CH_2—OOC), 3.75 (t, 2H N—*CH2*—CH_2—NHOC), 3.54 (t, 2H, CH_2—CH_2—N), 3.37 (s, 6H, N—CH_3), 1.94 (s, 3H, CH_3—C=C), 1.76 (m, 2H, —CH_2—CH_2—OOC), 1.67 (m, 2H, —CH_2—CH_2—N), and 1.24-1.44 (m,14H, —$(CH_2)_7$—). MALDI-TOF (positive ion): Calcd *m*/*z* for $C_{36}H_{47}O_3N_2^+$: 555.36; found, 555.47.

Synthesis of RhB-EO_4-N_3

RhB (0.48 g, 1.0 mmol) and EDCI (0.21 g, 1.1 mmol) were dissolved in 20-ml anhydrous DCM under the ice bath and stirred for 10 min. Then, NH_2-EO_4-N_3 (0.24 g, 1.1 mmol) and DMAP (6.11 mg, 0.05 mmol) were added. The solution was allowed to slowly rise to room temperature and reacted overnight in the dark. After that, the solution was concentrated, and the product was purified by column chromatography. RhB-EO_4-N_3 was obtained as a reddish-brown oil with a yield of 54%.

^{1}H NMR (500 MHz, $CDCl_3$): δ (ppm) 8.28 (d, 1H, Ph), 7.84 (t, 1H, Ph), 7.76 (t, 1H, Ph), 7.34 (d, 1H, Ph), 7.08 (d, 2H, Ph), 6.97 (d, 2H,

Ph), 6.84 (s, 2H, Ph), 3.76 to 3.48 (m, 14H, NH-($CH_2CH_2O)_3$—CH_2—; 8H, CH_3—CH_2—N), 3.41 (t, 2H, —CH_2—N_3), and 1.34 (t, 12H, CH_3—CH_2—N). MALDI-TOF (positive ion): Calcd m/z for $C_{36}H_{47}O_5N_6^+$: 643.36; found, 643.40.

Synthesis of Fls-EO_4-N_3

FITC (0.39 g, 1.00 mmol) was dissolved in 20-ml anhydrous DCM under the ice bath. Then, NH_2-EO_4-N_3 (0.24 g, 1.1 mmol) was added. The solution was allowed to slowly rise to room temperature and reacted overnight in the dark. After reaction, the solution was concentrated, and the product was purified by column chromatography. Fls-EO_4-N_3 was obtained as a brown oil with a yield of 41%.

^{1}H NMR (500 MHz, DMSO): δ (ppm) 8.30 (s, 1H, Ph), 7.75 (d, 1H, Ph), 7.17 (d, 1H, Ph), 6.67 (s, 2H, Ph), 6.57 (m, 4H, Ph), 3.70 to 3.45 (m, 14H, CSNH—($CH_2CH_2O)_3$—CH_2—), and 3.25 (t, 2H, —CH_2—N_3). MALDI-TOF (positive ion): Calcd m/z for $C_{29}H_{29}O_8N_5S$: 607.17; found, 608.21 (+H^+).

Synthesis of Pyr-EO_4-N_3

1-Pyrenecarboxylic acid (0.25 g, 1.0 mmol) and EDCI (0.21 g, 1.1 mmol) were dissolved in 30-ml anhydrous DCM under the ice bath and stirred for 10 min. Then, NH_2-EO_4-N_3 (0.24 g, 1.1 mmol) and DMAP (6.11 mg, 0.05 mmol) were added. The solution was allowed to slowly rise to room temperature and reacted 24 hours in the dark. After reaction, the solution was concentrated, and the product was purified by column chromatography. Pyr-EO_4-N_3 was obtained as a yellowish liquid with a yield of 38%.

^{1}H NMR (500 MHz, $CDCl_3$): δ (ppm) 9.27 (s, 1H, Ph), 8.67 (s, 1H, Ph), 8.30 to 8.05 (m, 7H, Ph), 3.80 to 3.50 [m, 14H, NH—($CH_2CH_2O)_3$—CH_2—], and 3.40 (t, 2H, —CH_2—N_3). MALDI-TOF (positive ion): Calcd m/z for $C_{25}H_{26}O_4N_4$: 446.20; found, 446.27 (+H^+).

Adsorption isotherm of MA-11-2-11-MA on silicon

The adsorption behavior of MA-11-2-11-MA at the solid-liquid interface play a critical role in the formation of the bilayer and the synthesis of *net*-poly(MA-11-2-11-MA). The adsorption isotherm of MA-11-2-11-MA at 65°C was studied with monocrystalline silicon powder (10 mg/ml), which had the same surface properties with the silicon wafer but a much larger specific surface area (21 m^2/g, according to the N_2 absorption-desorption isotherms obtained on a Quantachrome Nova 4200e at 77 K). The adsorption of MA-11-2-11-MA was detected by measuring the concentration change (ΔC) in solution using ^{1}H NMR (with an external standard capillary of DSS, 4,4-dimethyl-4-silapentane-1-sulfonic acid). The adsorption curve (fig. S1B), which is similar to that in the previous report (*33*), indicates the typical double-layer adsorption behavior of MA-11-2-11-MA on silicon powder. We calculate the packing density of MA-11-2-11-MA on silicon to be 3.81 molecule/nm^2 at full packing condition (C_{equ} = 4.34 mM). The relatively high packing density indicates a tight arrangement of MA-11-2-11-MA on silicon surface.

Preparation of *net*-poly(MA-11-2-11-MA) film on silicon wafer

A piece of silicon wafer (2.0 cm by 2.0 cm) was ultrasonically cleaned in acetone and DI water and boiled in the piranha solution. After rinsing with dilute NaOH solution (0.10 mM) to remove the acid residue, the silicon wafer was immersed in a solution of MA-11-2-11-MA (10 ml, 5.0 mM) at 45°C in a test tube. The solution was statically cooled to room temperature, degassed with nitrogen bubbling, and sealed up. Then, the solution was heated to 65°C for an incubation period of 10 min, and initiator ACVA (25 μl, 100 mM, degassed) was added. The polymerization was carried out at 65°C for 5 hours, and the resulting silicon wafer was rinsed gently with DI water to remove any residues. All the copolymerization procedures on silicon wafers and mica sheets in the rest of the paper were conducted under identical polymerization conditions as described above.

The clear edge of the *net*-poly(MA-11-2-11-MA) film (Fig. 1B) was prepared using oxygen RIE method. Specifically, as-prepared *net*-poly(MA-11-2-11-MA) film on silicon wafer was partly covered by a clean silicon wafer with a sharp and straight edge. Then, the film was etched with oxygen plasma gas for 60 s to remove the uncovered part of the film. Alternatively, a broken area of *net*-poly(MA-11-2-11-MA) film could be found after violently rinsing with DI water at the edge of the silicon wafer (fig. S2D), which can also be used to characterize the thickness of *net*-poly(MA-11-2-11-MA) film.

Molecular orientation of MA-11-2-11-MA in multilayer films

Multilayer films of MA-11-2-11-MA were prepared to enhance the infrared spectra signal according to the previous reports with slight modification (*34*). Specifically, a solution of MA-11-2-11-MA (5.0 ml, 5.0 mM) was sonicated at 45°C for 10 min. Then, a few drops of the solution were dropped onto a silver (100 μm thick) covered slide glass (for the grazing-angle reflection mode) or a calcium fluoride window (for the transmission mode), which were heated to 45°C in advance. The slide glass and the window sheet were placed in a capped petri dish with slight tilt in a hot oven at 45°C to slowly evaporate the solvent. Last, the slide glass and the window sheet were placed in a capped vial containing a few drops of water and incubated for 24 hours at 25°C. The optical texture in the polarizing light microscopy image of the prepared multilayer (fig. S3A) was consistent with the smectic phase, suggesting the multilayer films of MA-11-2-11-MA having a lamellar structure. The obtained infrared spectra in the two measure modes were shown after normalization (fig. S3B). Considering that there may be structural differences between multilayer films of MA-11-2-11-MA and *net*-poly(MA-11-2-11-MA) bilayers, this result should be regarded as qualitative explanations instead of an exact description of the molecular orientation.

DPD simulation of *net*-poly(MA-11-2-11-MA)

In the DPD, the time evolution of the interacting beads was governed by Newton's equations of motion (*35*). All the beads in the model are subject to three nonbonded pairwise forces, i.e., conservative force, dissipative force, and random force. The conservative force takes the form $\mathbf{F}_{ij}^C = \alpha_{ij}(1 - r_{ij}/r_c)\boldsymbol{e}_{ij}$, where α_{ij} is the repulsion strength between beads i and j, $\mathbf{e}_{ij} = \boldsymbol{r}_{ij}/r_{ij}$ with $\mathbf{r}_{ij} = \mathbf{r}_i - \mathbf{r}_j$ and $r_{ij} = |\boldsymbol{r}_{ij}|$. The dissipative force is $\mathbf{F}_{ij}^D = -\gamma\omega^D(r_{ij})(\mathbf{v}_{ij}\cdot\mathbf{e}_{ij})\mathbf{e}_{ij}$ and the random force is $\mathbf{F}_{ij}^R = \sigma\omega^R(r_{ij})\xi_{ij}\Delta t^{-1/2}\mathbf{e}_{ij}$, where $\mathbf{v}_{ij} = \mathbf{v}_i - \mathbf{v}_j$ and ξ_{ij} is a random number with zero mean and unit variance. The weight functions $\omega^D(r_{ij})$ and $\omega^R(r_{ij})$ were correlated with each other by $\omega^D(r_{ij}) = [\omega^R(r_{ij})]^2$, and the coefficients γ and $\sigma^2 = 2\gamma k_B T$ determine the strength of dissipative and random forces and form a thermostat (*36*). The bonds between beads in the polymer chain were represented by $\mathbf{F}_{ij}^S = -k_S\mathbf{r}_{ij}$ with a stiffness constant k_S = 10. In our simulations, the bead mass m, the radius of interaction cutoff r_c, and the energy [expressed by $k_B T$ (Boltzmann constant)] are set as the units, i.e., $m = r_c = k_B T = 1$. The time unit is therefore $\tau = \sqrt{(mr_c^2/k_B T)} = 1$. The integration time step in the simulation is Δt = 0.02, the number density is

$\rho_0 = 3$, and the friction parameter is $\gamma = 4.5$. Unless specified otherwise, all dimensional values were given in DPD units. In DPD, as in coarse-grained molecular dynamics simulation, the molecule was reduced by combining several atoms or atomic groups into CG (coarse-grain) particles that interact via an effective force field. In our simulations, water was represented by a yellow CG bead (S). Each MA-11-2-11-MA molecule was modeled as a three-component amphiphilic molecule consisting of blue hydrophilic beads (N), gray hydrophobic chains (C), and red tail reactive beads (O), as shown in Fig. 2A. The coarse-graining rules for monomeric MA-11-Me_3 were the same as that for MA-11-2-11-MA, except that the color of hydrophobic chains was changed to green for visual discrimination (fig. S7). Amphiphilicity was introduced by assigning different interaction parameters between different kinds of beads. The repulsion parameters α_{ij} used in this work are listed in table S1.

The initial model of the bilayer was constructed as two monolayers on the opposite sides of a slab of aqueous solution, and the thickness of the slab was enough to isolate the two monolayers effectively. Each monolayer initially is composed of 400 molecules uniformly distributed in the *x-y* plane of a 20 by 20 square box. The hydrophobic chains of the surfactant extend perpendicular to the *x-y* plane in all conformations, and the reactive beads at the chain ends distribute averagely in the middle of the surfactant bilayer. We introduce the concept of reaction probability to model the free-radical polymerization of vinyl groups, as used in the study of surface-initiated polymerization (*37*). In the simulations, the reaction probability was fixed at $P_r = 0.1$, and the reaction time interval was set as $t = 50$, $\Delta t = 1$.

The models were equilibrated in the first 2×10^6 time steps before the polymerization reaction was switched on. During the following 2×10^6 steps, the reaction was allowed to take place every 50 steps, and the data were collected every 1×10^4 steps for subsequent analysis. To improve the statistics, we ran six independent simulations for each system to calculate the mean value and the error bar. All the DPD simulations were performed using GALAMOST software package (*38*).

Fluorescent *net*-poly(MA-11-2-11-MA)-*co*-(MA-11-F) (F = RhB, Fls, or Pyr) film in letter shapes

Fluorescent *net*-poly(MA-11-2-11-MA)-*co*-(MA-11-F) (F = RhB, Fls, or Pyr) films on silicon wafers were prepared using standard conditions as described above. The fluorescent monomeric derivatives were copolymerized at a molar fraction of 10%. Three kinds of fluorescent film were prepared separately and patterned into letter shapes using oxygen RIE etching method with letter-shaped masks (the masks were fabricated by laser beam lithography with the size of each letter within 0.5 mm^2). Uncovered parts of the fluorescent film were removed.

Post-polymerization functionalization of *net*-poly(MA-11-2-11-MA)-*co*-(MA-11-C≡C) on silica wool

Silica wool (5.0 mg) was coated with *net*-poly(MA-11-2-11-MA)-*co*-(MA-11-C≡C) by copolymerization in 5.0-ml solution of MA-11-2-11-MA (5.0 mM), MA-11-C≡C (0.50 mM), and ACVA (0.25 mM). After the copolymerization at 65°C for 5 hours, the silica wool was rinsed with DI water and immersed in 5.0-ml solution of RhB-EO_4-N_3 [or Fls-EO_4-N_3, Pyr-EO_4-N_3, (1.0 mM), and $CuSO_4$ (0.10 mM)] in a test tube under nitrogen atmosphere. A solution of sodium ascorbate (100 μl, 10 mM, degassed) was injected into the test tube, and the reaction was kept in the dark for 24 hours at room temperature. The produced silica wool was rinsed with DI water to wash off the floating color.

Preparation of *net*-poly(MA-11-2-11-MA)-*co*-(MA-11-RhB) capsules

Silica microrods and microboards were synthesized according to previous reports (*39*, *40*). Silica microspheres were commercially purchased. Approximately 1.0 mg of each silica microparticle (i.e., microspheres, microrods, and microboards) was washed twice with DI water in a centrifugal tube. A solution (10 ml, 45°C) of MA-11-2-11-MA (5.0 mM) and MA-12-RhB (0.50 mM) was injected into the centrifugal tube under ultrasonic. The mixed solution was then cooled to room temperature, transferred to a test tube containing the initiator ACVA (25 μl, 100 mM), and degassed with nitrogen bubbling. The polymerization was carried out at 65°C for 5 hours, and the obtained microparticles were washed twice with DI water.

The capsules of *net*-poly(MA-11-2-11-MA)-*co*-(MA-11-RhB) were prepared by etching the silica microparticles with hydrofluoric acid solution (2 wt %). TEM energy dispersive spectrometry confirmed the completely removal of silica microparticles (with capsules from microrod templates as an example; fig. S9A).

The silica microrods were partially hydrolyzed when heated in aqueous solution. Therefore, one side of the silica microrod was relative more porous (fig. S9B), resulting in the capsules with a deeper contrast in TEM images (Fig. 5B and fig. S9C) and brighter fluorescence in fluorescence microscope images (Fig. 5E) on the porous side.

Coating macroscale objects with fluorescent 2D copolymer

Quartz cuvette and copper coin were ultrasonically cleaned in acetone and water. Polystyrene petri dish was heated in concentrated sulfuric acid at 60°C for 20 min for sulfonation and then rinsed with dilute NaOH solution (0.10 mM) to remove the acid residue. Above macroscale objects were coated with *net*-poly(MA-11-2-11-MA)-*co*-(MA-11-RhB) by copolymerization in a solution of MA-11-2-11-MA (5.0 mM), MA-11-RhB (0.50 mM), and ACVA (0.25 mM) at 65°C for 5 hours.

Antibacterial assay of cotton gauze

Cotton gauze was ultrasonically cleaned in ethanol and water, and then coated with *net*-poly(MA-11-2-11-MA)-*co*-(MA-11-RhB). After copolymerization in a solution of MA-11-2-11-MA (5.0 mM), MA-11-RhB (0.50 mM), and ACVA (0.25 mM) at 65°C for 5 hours, the gauze was rinsed thoroughly with DI water to wash off any unreacted residue (Fig. 6B). Then, the coated cotton gauze as well as untreated cotton gauze serving as a control were taken 0.25 g of each and immersed completely in 1.0-ml *S. aureus* suspension (1×10^5 colony-forming units/ml). After culturing at 37°C for 24 hours, the gauzes were taken out and washed with phosphate-buffered saline (PBS) buffer solution to remove the floating *S. aureus*. The gauzes were then ultrasonically treated in a PBS buffer solution (2.0 ml) for 10 min to release the adherent *S. aureus*. The released *S. aureus* suspension was diluted for a series of times and cultured at 37°C for 24 hours.

SUPPLEMENTARY MATERIALS

Supplementary material for this article is available at http://advances.sciencemag.org/cgi/content/full/5/11/eaaw9120/DC1

Fig. S1. The CMC and the adsorption behavior of MA-11-2-11-MA.

Fig. S2. Preparation of *net*-poly(MA-11-2-11-MA) on the silicon wafer.

Fig. S3. Molecular orientation of MA-11-2-11-MA in multilayer films.

Fig. S4. XPS spectra of C1s of *net*-poly(MA-11-2-11-MA).
Fig. S5. AFM indentation experiments on 2D *net*-poly(MA-11-2-11-MA).
Fig. S6. NMR characterization of individually dispersed MA-11-2-11-MA.
Fig. S7. DPD simulation of *net*-poly(MA-11-2-11-MA)-*co*-(MA-11-2-Me_3).
Fig. S8. Functionalization of 2D *net*-poly(MA-11-2-11-MA).
Fig. S9. Preparation of the *net*-poly(MA-11-2-11-MA)-*co*-(MA-11-RhB) capsules.
Table S1. Repulsion parameters used in the DPD simulations.

REFERENCES AND NOTES

1. Y. Zang, T. Aoki, M. Teraguchi, T. Kaneko, L. Ma, H. Jia, Two-dimensional and related polymers: Concepts, synthesis, and their potential application as separation membrane materials. *Polym. Rev.* **55**, 57–89 (2015).
2. D. Rodríguez-San-Miguel, P. Amo-Ochoa, F. Zamora, MasterChem: Cooking 2D-polymers. *Chem. Commun.* **52**, 4113–4127 (2016).
3. Z. Xiang, D. Cao, L. Dai, Well-defined two dimensional covalent organic polymers: Rational design, controlled syntheses, and potential applications. *Polym. Chem.* **6**, 1896–1911 (2015).
4. J. Sakamoto, J. van Heijst, O. Lukin, A. D. Schlüter, Two-dimensional polymers: Just a dream of synthetic chemists? *Angew. Chem. Int. Ed.* **48**, 1030–1069 (2009).
5. M. Servalli, A. D. Schlüter, Synthetic two-dimensional polymers. *Annu. Rev. Mater. Res.* **47**, 361–389 (2017).
6. W. Wang, A. D. Schlüter, Synthetic 2D polymers: A critical perspective and a look into the future. *Macromol. Rapid Commun.* **40**, 1800719 (2019).
7. S. I. Stupp, S. Son, H. C. Lin, L. S. Li, Synthesis of two-dimensional polymers. *Science* **259**, 59–63 (1993).
8. H. Ringsdorf, B. Schlarb, J. Venzmer, Molecular architecture and function of polymeric oriented systems: models for the study of organization, surface recognition, and dynamics of biomembranes. *Angew. Chem. Int. Ed. Engl.* **27**, 113–158 (1988).
9. T. M. Sisson, H. G. Lamparski, S. Kölchens, A. Elayadi, D. F. O'Brien, Cross-linking polymerizations in two-dimensional assemblies. *Macromolecules* **29**, 8321–8329 (1996).
10. K. Morigaki, K. Kiyosue, T. Taguchi, Micropatterned composite membranes of polymerized and fluid lipid bilayers. *Langmuir* **20**, 7729–7735 (2004).
11. T. Okazaki, T. Inaba, Y. Tatsu, R. Tero, T. Urisu, K. Morigaki, Polymerized lipid bilayers on a solid substrate: Morphologies and obstruction of lateral diffusion. *Langmuir* **25**, 345–351 (2009).
12. P. Payamyar, B. T. King, H. C. Öttinger, A. D. Schlüter, Two-dimensional polymers: Concepts and perspectives. *Chem. Commun.* **52**, 18–34 (2016).
13. M. Trenary, Reflection absorption infrared spectroscopy and the structure of molecular adsorbates on metal surfaces. *Annu. Rev. Phys. Chem.* **51**, 381–403 (2000).
14. E. Okamura, J. Umemura, T. Takenaka, Orientation studies of hydrated dipalmitoylphosphatidylcholine multibilayers by polarized FTIR-ATR spectroscopy. *Biochim. Biophys. Acta Biomembr.* **1025**, 94–98 (1990).
15. C. Lee, X. Wei, J. W. Kysar, J. Hone, Measurement of the elastic properties and intrinsic strength of monolayer graphene. *Science* **321**, 385–388 (2008).
16. S. Bertolazzi, J. Brivio, A. Kis, Stretching and breaking of ultrathin MoS_2. *ACS Nano* **5**, 9703–9709 (2001).
17. N. Zhang, T. Wang, X. Wu, C. Jiang, T. Zhang, B. Jin, H. Ji, W. Bai, R. Bai, From 1D polymers to 2D polymers: Preparation of free-standing single-monomer-thick two-dimensional conjugated polymers in water. *ACS Nano* **11**, 7223–7229 (2017).
18. R. Zana, Dimeric and oligomeric surfactants. Behavior at interfaces and in aqueous solution: A review. *Adv. Colloid Interface Sci.* **97**, 205–253 (2002).
19. S. Manne, T. E. Schäffer, Q. Huo, P. K. Hansma, D. E. Morse, G. D. Stucky, I. A. Aksay, Gemini surfactants at solid-liquid interfaces: Control on interfacial aggregate geometry. *Langmuir* **13**, 6382–6387 (1997).
20. F. P. Duval, R. Zana, G. G. Warr, Adsorbed layer structure of cationic gemini and corresponding monomeric surfactants on mica. *Langmuir* **22**, 1143–1149 (2006).
21. K. Tajima, T. Aida, Controlled polymerizations with constrained geometries. *Chem. Commun.*, 2399–2412 (2000).
22. M. Beiner, H. Huth, Nanophase separation and hindered glass transition in side-chain polymers. *Nat. Mater.* **2**, 595–599 (2003).
23. A. S. Doost, M. Akbari, C. V. Stevens, A. D. Setiowati, P. Van der Meeren, A review on nuclear overhauser enhancement (NOE) and rotating-frame overhauser effect (ROE) NMR techniques in food science: Basic principles and applications. *Trends Food Sci. Technol.* **86**, 16–24 (2019).
24. J. López-Cabrelles, S. Mañas-Valero, I. J. Vitórica-Yrezábal, P. J. Bereciartua, J. A. Rodríguez-Velamazán, J. C. Waerenborgh, B. J. C. Vieira, D. Davidovikj, P. G. Steeneken, H. S. J. van der Zant, G. Mínguez Espallargas, E. Coronado, Isoreticular two-dimensional magnetic coordination polymers prepared through pre-synthetic ligand functionalization. *Nat. Chem.* **10**, 1001–1007 (2018).
25. L. Xu, L. Cao, Z. Guo, Z. Zha, S. Lei, Side-functionalized two-dimensional polymers synthesized *via* on-surface Schiff-base coupling. *Chem. Commun.* **51**, 8664–8667 (2015).
26. G. M. Ziarani, Z. Hassanzadeh, P. Gholamzadeh, S. Asadia, A. Badiei, Advances in click chemistry for silica-based material construction. *RSC Adv.* **6**, 21979–22006 (2016).
27. J. Cui, M. P. van Koeverden, M. Müllner, K. Kempe, F. Caruso, Emerging methods for the fabrication of polymer capsules. *Adv. Colloid Interface Sci.* **207**, 14–31 (2014).
28. S. H. Behrens, D. G. Grier, The charge of glass and silica surfaces. *J. Chem. Phys.* **115**, 6716–6721 (2001).
29. M. N. Shalaby, M. M. Osman, Protection of copper surface against corrosion by cationic surfactant in seawater. *J. Disper. Sci. Technol.* **30**, 677–683 (2009).
30. M. Hazarika, K. Malkappa, T. Jana, Particle-size-dependent properties of sulfonated polystyrene nanoparticles. *Polym. Int.* **61**, 1425–1432 (2012).
31. L. Caillier, E. T. de Givenchy, R. Levy, Y. Vandenberghe, S. Geribaldi, F. Guittard, Polymerizable semi-fluorinated gemini surfactants designed for antimicrobial materials. *J. Colloid Interface Sci.* **332**, 201–207 (2009).
32. M. Abe, K. Tsubone, T. Koike, K. Tsuchiya, T. Ohkubo, H. Sakai, Polymerizable cationic gemini surfactant. *Langmuir* **22**, 8293–8297 (2006).
33. C. Chorro, M. Chorro, O. Dolladille, S. Partyka, R. Zana, Adsorption of dimeric (gemini) surfactants at the aqueous solution/silica interface. *J. Colloid Interface Sci.* **199**, 169–176 (1998).
34. R. P. Richter, R. Bérat, A. R. Brisson, Formation of solid-supported lipid bilayers: An integrated view. *Langmuir* **22**, 3497–3505 (2006).
35. R. D. Groot, P. B. Warren, Dissipative particle dynamics: Bridging the gap between atomistic and mesoscopic simulation. *J. Chem. Phys.* **107**, 4423–4435 (1997).
36. P. Español, P. Warren, Statistical mechanics of dissipative particle dynamics. *Europhys. Lett.* **30**, 191–196 (1995).
37. H. Liu, M. Li, Z.-Y. Lu, Z.-G. Zhang, C.-C. Sun, T. Cui, Multiscale simulation study on the curing reaction and the network structure in a typical epoxy system. *Macromolecules* **44**, 8650–8660 (2011).
38. Y.-L. Zhu, H. Liu, Z.-W. Li, H.-J. Qian, G. Milano, Z.-Y. Lu, GALAMOST: GPU-Accelerated Large-Scale Molecular Simulation Toolkit. *J. Comput. Chem.* **34**, 2197–2211 (2013).
39. Y. Yang, H. Pei, G. Chen, K. T. Webb, L. J. Martinez-Miranda, I. K. Lloyd, Z. Lu, K. Liu, Z. Nie, Phase behaviors of colloidal analogs of bent-core liquid crystals. *Sci. Adv.* **4**, eaas8829 (2018).
40. Y. Yang, G. Chen, S. Thanneeru, J. He, K. Liu, Z. Nie, Synthesis and assembly of colloidal cuboids with tunable shape biaxiality. *Nat. Commun.* **9**, 4513 (2018).

Acknowledgments: We acknowledge the support of the State Key Laboratory of Supramolecular Structure and Materials. **Funding:** K.L. and Z.L. thank the National Natural Science Foundation of China (21534004) for financial support. K.L. gratefully acknowledges financial support from the National Natural Science Foundation of China (21634004). K.L. thanks the Opening funds of State Key Laboratory of Applied Optics, Changchun Institute of Optics, Fine Mechanics and Physics, Chinese Academy of Sciences for financial support. **Author contributions:** Y.L., Hua Yu, and Y.Y. carried out the synthesis work. Y.L., K.J., Y.S., and W.Z. performed the AFM measurement. H.G. and Z.L. performed the simulation work, Y.L., Huan Yu, and H.S. carried out the antibacterial test. All authors discussed the results. Y.L. and K.L. wrote the paper. **Competing interests:** The authors declare that they have no competing interests. **Data and materials availability:** All data needed to evaluate the conclusions in the paper are present in the paper and/or the Supplementary Materials. Additional data related to this paper may be requested from the authors.

Submitted 10 February 2019
Accepted 30 September 2019
Published 22 November 2019
10.1126/sciadv.aaw9120

Citation: Y. Li, H. Gao, H. Yu, K. Jiang, H. Yu, Y. Yang, Y. Song, W. Zhang, H. Shi, Z. Lu, K. Liu, Two-dimensional polymers with versatile functionalities via gemini monomers. *Sci. Adv.* **5**, eaaw9120 (2019).

Science Advances

Two-dimensional polymers with versatile functionalities via gemini monomers

Yang Li, Huimin Gao, Huan Yu, Ke Jiang, Hua Yu, Yang Yang, Yu Song, Wenke Zhang, Hengchong Shi, Zhongyuan Lu and Kun Liu

Sci Adv **5** (11), eaaw9120.
DOI: 10.1126/sciadv.aaw9120